CHEMISTRY OF MATERIALS
Cite This: Chem. Mater. 2018, 30, 1249−1256
Article
pubs.acs.org/cm

Popcorn-Shaped Fe_xO (Wüstite) Nanoparticles from a Single-Source Precursor: Colloidal Synthesis and Magnetic Properties

Christoph P. Guntlin,[†,§] Stefan T. Ochsenbein,[†,§] Michael Wörle,[†] Rolf Erni,[‡] Kostiantyn V. Kravchyk,[†,§] and Maksym V. Kovalenko*[,†,§]

[†]Laboratory for Inorganic Chemistry, Department of Chemistry and Applied Biosciences, ETH Zürich, Vladimir Prelog Weg 1, CH-8093 Zürich, Switzerland

[§]Laboratory for Thin Films and Photovoltaics and [‡]Electron Microscopy Center, EMPA−Swiss Federal Laboratories for Materials Science and Technology, Überlandstrasse 129, CH-8600 Dübendorf, Switzerland

Supporting Information

ABSTRACT: Colloidal nanoparticles (NPs) with myriads of compositions and morphologies have been synthesized and characterized in recent years. For wüstite Fe_xO, however, obtaining phase-pure NPs with homogeneous morphologies have remained challenging. Herein, we report the colloidal synthesis of phase-pure Fe_xO ($x \approx 0.94$) popcorn-shaped NPs by decomposition of a single-source precursor, $[Fe_3(\mu_3\text{-}O)(CF_3COO)(\mu\text{-}CF_3COO)_6(H_2O)_2]\cdot CF_3COOH$. The popcorn shape and multigrain structure had been reconstructed using high-angle annular dark-field scanning transmission electron micrograph (HAADF-STEM) tomography. This morphology offers a large surface area and internal channels and prevents further agglomeration and thermal tumbling of the subparticles. $[Fe_3(\mu_3\text{-}O)(CF_3COO)(\mu\text{-}CF_3COO)_6(H_2O)_2]\cdot CF_3COOH$ behaves as an antiferromagnetic triangle whose magnetic frustration is mitigated by the low symmetry of the complex. The popcorn-shaped Fe_xO NPs show the typical wüstite antiferromagnetic transition at approximately 200 K, but behave very differently to their bulk counterpart below 200 K. The magnetization curves show a clear, unsymmetrical hysteresis, which arises from a combined effect of the superparamagnetic behavior and exchange bias.

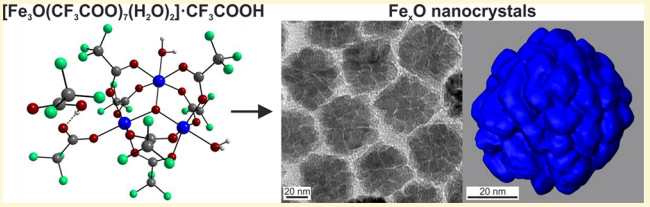

INTRODUCTION

Broadening the toolbox for the rational synthesis of nanomaterials is currently one of the most important objectives in inorganic chemistry. Nanosized materials such as NPs, have shown properties (optical, magnetic, and electronic) and possess attributes (colloidal state, tunable surface chemistry, etc.) that can benefit fields including bioimaging,[1] radiation detection,[2] light emission,[3] electrochemical energy storage,[4] photovoltaics,[5] and many more. State-of-the-art synthetic methods set high standards in the uniformity of the size, shape, and composition of NPs in a colloidal ensemble.

Wüstite Fe_xO (in general $x = 0.84$−0.95), an antiferromagnetic compound, crystallizes in a NaCl-type defective crystal structure. The stoichiometric composition (FeO) does not exist at ambient pressure and room temperature (RT). All obtained substoichiometric wüstite phases have a deficiency of iron, and hence the mixed valency ($Fe^{2+/3+}$) is necessary to maintain charge balance. Fe^{3+} cations move to unoccupied tetrahedral sites in Fe_xO, leaving behind vacancies on octahedral sites.[6] According to the phase diagram, bulk Fe_xO disproportionates into Fe_3O_4 and Fe below 570 °C. However, this disproportionation reaction becomes immeasurably slow below 300 °C.[7] Thus, Fe_xO exists as a metastable phase at room temperature.[6,8] Yin and ÒBrien[9] showed that colloidal wüstite NPs can be synthesized at 320 °C due to the already strongly reduced rate of redox disproportionation close to 300 °C. Thus, Fe_xO is kinetically stable at RT in bulk and as NPs.[10] Fe_xO NPs are expected to be faster oxidized in air as compared to the bulk due to their larger surface area. However, fast oxidation is generally not observed, and the oxidation rates strongly depend on the capping ligands and the particle sizes/morphology. Thus, oxidation can be slow and occurs mostly on the surface, leading to a ferromagnetic shell covering the antiferromagnetic wüstite core.[11−13] Previously, Fe_xO NPs with shapes such as spheres, cubes, octapods, and truncated octahedra[9,14−18] were synthesized. Typically, single-source precursors such as iron(II) acetate,[9,14,18] or $Fe(acac)_{2-3}$,[14,15] or long-chain carboxylates[16,17] are decomposed in high boiling solvents or by selective oxidation of $Fe(CO)_5$ with pyridine N-oxide.[14] Another approach is to decompose Fe-oleates, leading to a wide variety of NP shapes[16,17] and allowing the synthesis of heterostructures such as wüstite/spinel[19] or wüstite/ferrite[20,21] core−shell NPs. However, a clean wüstite phase has scarcely been obtained at NP sizes below ∼20 nm because of the aforementioned surface oxidation of Fe_xO and the limitations of these precursors in producing only Fe^{2+} species.

In this report, we present a synthesis of novel, popcorn-shaped Fe_xO ($x \approx 0.94$) NPs (Figure 1), with high structural

Received: October 18, 2017
Revised: January 22, 2018
Published: January 25, 2018

DOI: 10.1021/acs.chemmater.7b04382
Chem. Mater. 2018, 30, 1249−1256

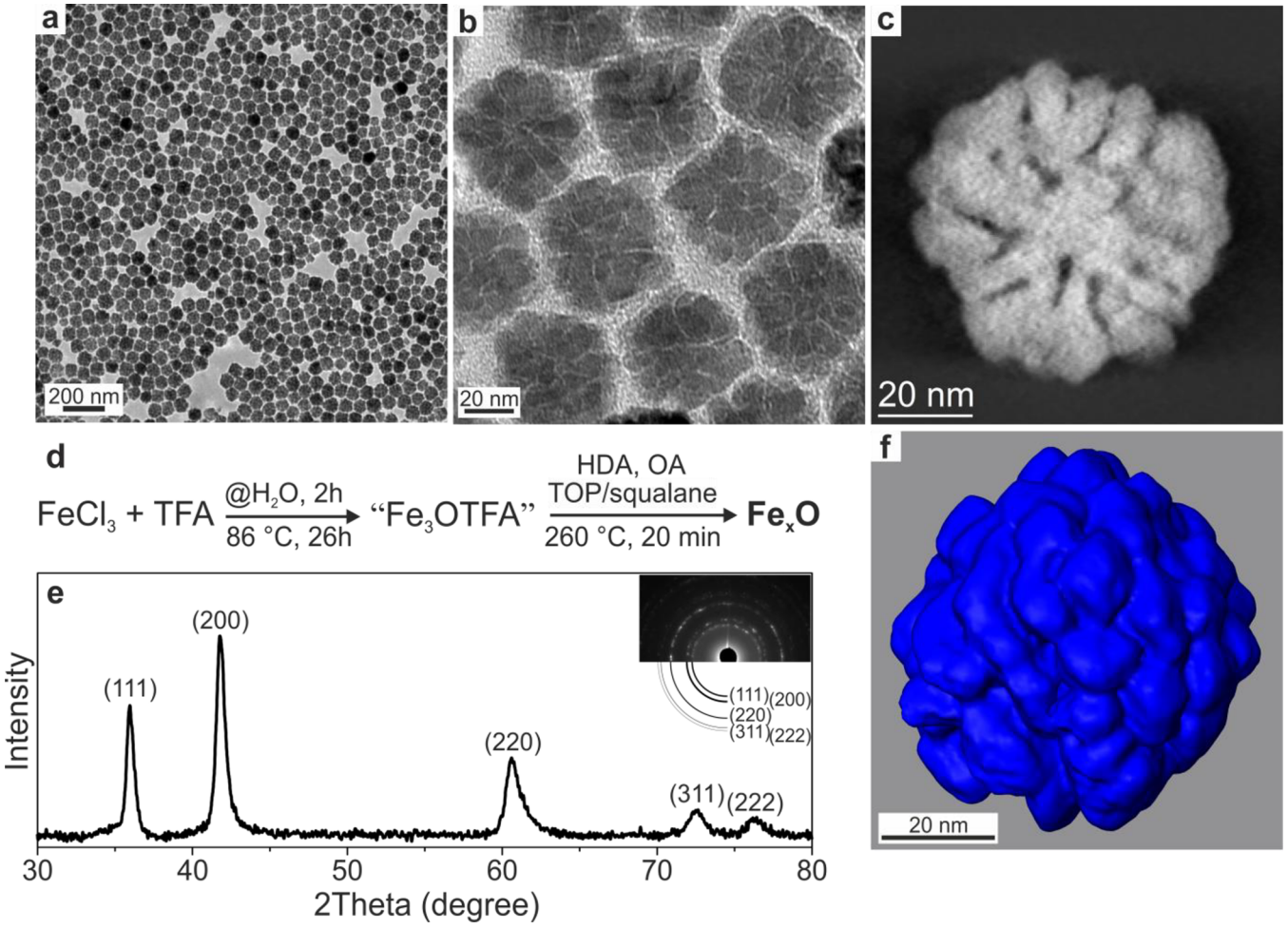

Figure 1. Structural characterization of popcorn-shaped Fe_xO NPs ($x \approx 0.94$): (a, b) overview TEM images, (c) slice through the reconstructed HAADF-STEM tomogram, (d) reaction scheme for the NP synthesis, and (e) powder XRD (Cu Kα_1, 1.540598 Å); inset: SAED spectrum of Fe_xO NPs. (f) 3D tomography image reconstructed by tilt-series of HAADF-STEM images.

and size uniformity. The synthesis decomposes an iron(III) oxo-trifluoroacetate single-source precursor (denoted as "Fe_3OTFA") in squalane as an inert solvent together with trioctylphosphine (TOP) as a mild reductant and capping agent and oleic acid (OA) and hexadecylamine (HDA) as capping ligands. The composition of the Fe_xO NPs with $x \approx 0.94$ was elucidated by a Rietveld refinement of a powder XRD pattern and by elemental mapping on the atomic scale using analytical electron microscopy. We also detail the crystal structures of the main precursor and three additional iron trifluoroacetate complexes discovered in this work. Additionally, the magnetic properties of the synthesized Fe_xO NPs and their precursor are presented and discussed.

EXPERIMENTAL SECTION

Synthesis of "Fe_3OTFA" Precursor. Ten grams (62 mmol) of $FeCl_3$ (Alfa Aeser, 98%) were mixed with trifluoroacetic acid (100 mL, 1.3 mol, TFA, Fischer) in a 250 mL two-neck round-bottom flask under N_2 flow and degassed three times by applying vacuum. Subsequently, the reaction mixture was heated to 86 °C and left stirring for 2 h until a homogeneous yellow suspension was obtained. Then 1 mL of deionized water was injected, quickly turning the color of suspension into a dark red. The solution was left stirring for additional 24 h at 86 °C. After cooling, TFA excess was distillated off under vacuum. The remaining solid product, "Fe_3OTFA", was dried at 60 °C under vacuum for at least 5 h, yielding a fine red powder, which is directly useable without further workup. Despite "Fe_3OTFA" appearing stable under ambient atmosphere, it was stored under vacuum until further use.

Synthesis of Popcorn-Shaped Fe_xO ($x \approx 0.94$) NPs. In a typical synthesis, "Fe_3OTFA" (337 mg, 0.3 mmol) was mixed with HDA (1.304 g, 5.4 mmol, Aldrich, 90%), squalene (5 mL, Merck, ≥ 99%), OA (3.6 mmol, 1.143 mL, Aldrich, 90%), TOP (5 mL, Strem, 15−6655, > 97%) in a 25 mL three-neck round-bottom flask, forming a dark solution. This mixture was degassed by alternating between vacuum and N_2 flow for 3 times at room temperature, followed by heating under vacuum to 110 °C and left drying for another 1.5 h. Afterward, the mixture was heated (19 °C/min) to 260 °C under N_2. At ca. 210 °C, the solution changed color from black to a clear, light yellow. Subsequent NC nucleation and growth processes were visible as a color change from light yellow via brown to black at 260 °C. After 20 min at 260 °C, the solution was rapidly cooled to 110 °C and 20 mL of toluene were added, followed by complete cooling. For purifying the particles, the reaction mixture was mixed with 30 mL of ethanol as a nonsolvent and centrifuged (8000 rpm, 3 min), the supernatant was discarded and the precipitate was dispersed in 10 mL of toluene.

Materials Characterization. Low and high resolution transmission electron microscopy images (LRTEM/HRTEM) as well as selected area electron diffraction (SAED) patterns were obtained with a JEOL JEM-2200FS microscope operating at 200 kV. NCs were deposited onto a carbon-coated Cu grids (Ted-Pella). A tomographic tilt-series from −76 to 72° (2° steps) were recorded on an STEM-aberration-corrected FEI Titan Themis operated at 300 kV with a

DOI: 10.1021/acs.chemmater.7b04382
Chem. Mater. 2018, 30, 1249−1256

probe semiconvergence angle of 18 mrad (beam current 70 pA). The limits of the angular tilt-range were given by shadowing of the Cu grid. The tomogram was reconstructed based on high-angle annular dark-field scanning transmission electron micrographs using FEI's Inspect3D, and visualized using Amira software. For element mapping using high-angle annular dark-field scanning transmission (HAADF-STEM) electron microscopy, combined with energy dispersive X-ray spectroscopy (EDX), a beam current of 6 nA (no difference with 1 or 3 nA) and detection with a SuperEDX system (4 detectors) were used. Powder X-ray diffraction (XRD) patterns were obtained on a Stoe STADI P powder X-ray diffractometer (Cu $K\alpha_1$ radiation, λ = 1.540598 Å, germanium monochromator). The powders were measured on a transmission sample holder or in a capillary (0.5 mm, Hilgenberg). For single-crystal measurements, a suitable crystal was selected and tip-mounted either on a Bruker SMART platform with an Apex I-detector diffractometer for "Fe_3OTFA" at 250 K or on a Bruker D8 SMART platform equipped with an Apex II detector for the other structures at 100 or 250 K using graphite-monochromated Mo Kα radiation (λ = 0.71073 Å). Using Olex2,[22] the structure was solved with the ShelXD[23] structure solution program using Dual Space or with the Superflip[24−26] structure solution program using charge flipping and refined with the ShelXL[27] refinement package using least-squares minimization. Thermogravimetric analysis (TGA) coupled to mass spectrometry (MS) was performed using a Netzsch simultaneous thermal analyzer (STA 449 F5 Jupiter) coupled (tubes at 200 °C) with a quadrupole mass spectrometer (QMS 403 D Aëolos). "Fe_3OTFA" (13.1 mg) was placed in an aluminum crucible and heated under Ar gas flow (40 mL min^{-1}) to 500 °C (5 °C min^{-1}). Fourier transform infrared spectroscopy (FTIR) was measured on a Thermo Scientific Nicolet iS5 with an iD5 ATR accessory (diamond). The device is located in an argon glovebox (O_2 < 0.1 ppm, H_2O < 0.1 ppm).

Magnetic Measurements. The magnetic properties were measured on a Quantum Design PPMS-9. The magnetic susceptibility data of "Fe_3OTFA" were measured in an applied magnetic field of 0.1 T between 2 and 300 K after cooling the sample in zero field. The temperature-dependence of the magnetization of Fe_xO NPs was measured between 2 and 300 K in a field of 0.1 T after cooling without an applied field (zero-field cooled, ZFC) and after cooling in a magnetic field of 0.1 T (field cooled, FC). The field-dependence of the magnetization of Fe_xO NPs was measured at 2 K after cooling in zero-field, and at 2, 10, 50, 100, 200, and 300 K after cooling to 2 K in a field of 1 T.

RESULTS AND DISCUSSION

A direct and reproducible synthesis of a single-source precursor is the backbone of a successful nanoparticle synthesis method. For the presented synthesis of wüstite NPs, the precursor quality has a direct influence on the phase purity, size and shape of the Fe_xO NPs. A compound obtained by reacting $FeCl_3$ with TFA under reflux yields has been used as a catalyst in several organic syntheses.[28−35] Our investigation of this reaction identified a mixture of several products (Figures S1−S4, Tables S1−S8). Instead, $[Fe_3(\mu_3\text{-}O)(CF_3COO)(\mu\text{-}CF_3COO)_6(H_2O)_2]\cdot CF_3COOH$ as a single product was obtained in this work when the synthesis was modified by adding a defined amount of water at a later stage of the reaction. The phase-pure precursor was synthesized by reacting commercial $FeCl_3$ and TFA at 86 °C for 26 h with the injection of water after 2 h. After evaporation of the residual TFA, the precursor was obtained as a red, air-stable powder and used for the synthesis of wüstite NPs without further purification. We hypothesize that water ensures sufficient level of hydrolysis of the preformed, suspended $Fe(TFA)_3$. Instead of adding water, $FeCl_3\cdot 6H_2O$ as a starting reagent also yields an identical precursor. However, the wüstite NPs obtained from a precursor produced by water-assisted synthesis were substantially more uniform and reproducible. The crystal structure of our precursor, denoted as "Fe_3OTFA", was determined using single-crystal XRD (see Figure 2a and the Supporting Information for all the crystallographic details) and has an overall composition of $[Fe_3(\mu_3\text{-}O)(CF_3COO)(\mu\text{-}CF_3COO)_6(H_2O)_2]\cdot CF_3COOH$ (Figure 2a and Figure S1 and Tables S1 and S2). The powder XRD pattern indicates phase purity (Figure 2b). "Fe_3OTFA" crystallizes in the monoclinic space group $P2_1/n$. Three Fe^{3+} ions are arranged in a triangle around a central oxygen atom. Each side of the triangle comprises two bridging trifluoroacetates. Trans to the central oxygen atom, the sixth coordination site of the octahedral coordinated Fe^{3+} ions is occupied either by H_2O (2x) or by a trifluoroacetate. This trifluoroacetate group forms a hydrogen bond to a TFA molecule. This "Fe_3OTFA" and another earlier published structure[36] are the only known compounds with exclusively Fe^{3+} ions in the triangular core unit. Typically, this unit has only been observed with mixed ($Fe^{2+/3+}$) valency.[37−39] "Fe_3OTFA" is isostructural to $[Cr_3(\mu_3\text{-}O)(CF_3COO)_6(H_2O)_2(CF_3COO)]\cdot CF_3COOH$.[38] To elucidate the decomposition of "Fe_3OTFA", a TGA-MS analysis was conducted (Figure S5). In addition to the structure of "Fe_3OTFA", three additional crystal structures were obtained by varying the growth conditions of the single-crystal or by reducing the synthesis temperature. All three structures and the crystallographic details are presented in the Figures S2−S4 and Tables S3−S8. In this report, we focus exclusively on "Fe_3OTFA" as a precursor for the synthesis of wüstite NPs, because this compound can be obtained in high yield without further purification.

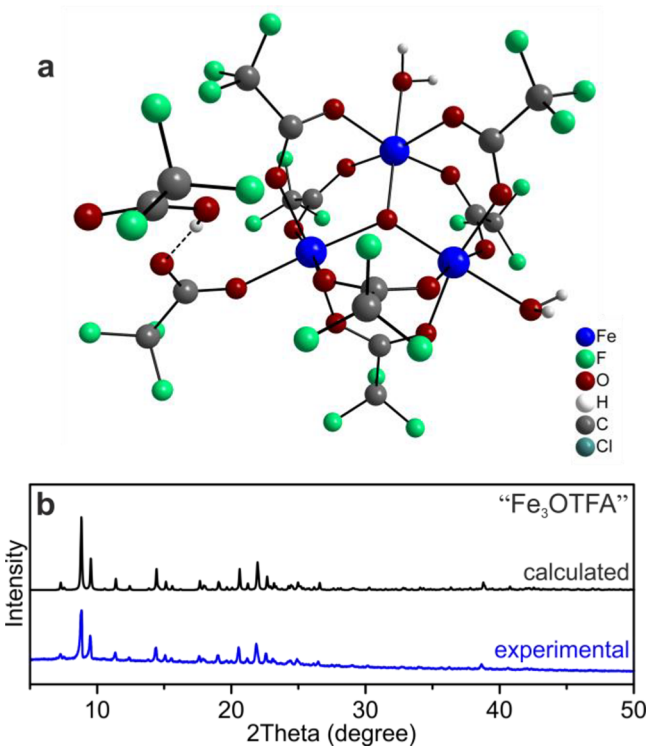

Figure 2. Structural analysis of the precursor: (a) the crystal structure of $[Fe_3(\mu_3\text{-}O)(CF_3COO)(\mu\text{-}CF_3COO)_6(H_2O)_2]\cdot CF_3COOH$ as obtained from the single-crystal XRD and (b) simulated and experimentally measured powder XRD patterns of this compound indicating the excellent phase purity of the precursor.

DOI: 10.1021/acs.chemmater.7b04382
Chem. Mater. 2018, 30, 1249−1256

Popcorn-shaped Fe_xO ($x \approx 0.94$) NPs (Figure 1a–c,f) were synthesized in a colloidal heating-up synthesis method at 260 °C (heating rate: ~19 °C/min) by decomposing "Fe_3OTFA" in TOP/squalane (1:1 by mass), HDA and OA under N_2. The starting solution had a dark-red to black appearance. It turned into a clear, slightly yellowish solution at approximately 210 °C. A subsequent color change to brown and then to metallic black indicated the nucleation and growth of NPs, respectively. The growth was finished when the solution turned shiny black. A reaction temperature of 260 °C for 20 min and a 12:18:1 OA:HDA:"Fe_3OTFA" molar ratio yielded the best size homogeneity. The size of the popcorn Fe_xO NP clusters is slightly tunable by varying the precursor amount between 0.3 and 0.4 mmol (Figure S6). Higher precursor amounts led to inhomogeneous size distributions. For the synthesis of popcorn-shaped Fe_xO NPs, obtaining the correct HDA/OA molar ratio and molar quantity is crucial. The molar ratio has to be between 1.3 and 2 (HDA/OA), and at least a 6-fold molar excess of OA to "Fe_3OTFA" is needed. When the HDA amount is increased to a 22-fold excess, the resulting Fe_xO NPs are separated, and no popcorn clusters are built (Figure S7). The growth mechanism of such polycrystalline popcorn-shaped NPs might first involve the formation of small (sub-10 nm) nuclei, which then aggregate into polycrystalline NPs. Such aggregation might be caused by the reduced solubility of NPs as they grow. The temperature at which the process occurs is presumably too low to cause efficient fusion of these crystalline domains.

The surface of the isolated Fe_xO NPs appears to be covered exclusively by oleates, according to FTIR (Figure S8). TOP is known as an efficient phosphor source[40] and hence might contaminate the oxide. This possibility had been ruled-out by high-resolution elemental mapping of Fe_xO NP using EDX measurements in HAADF-STEM mode (Figure 3). A very small phosphide signal indicates no distinct P surface shell, but at most a minute residual contamination. The growth of the popcorn shape may be influenced by three ligands: OA, HDA and an amide. The formation of the latter might be catalyzed in situ by Fe^{3+} ions.[41,42] When adding "Fe_3OTFA" only after the drying step (110 °C, 1.5 h, Figure S9), no popcorn-shaped Fe_xO NPs are obtained, which supports the assertion that Fe^{3+}-catalyzed amide formation is crucial to obtaining the popcorn-shape. The role of such a NP-yielding side reaction, whether by the amide as a ligand or a fluorine radical trap or by inducing a structural change in "Fe_3OTFA", remains uncertain. To obtain the wüstite phase, all four reactants (HDA, OA, TOP, and squalene) are needed, which was verified by excluding them one by one. The decomposition of "Fe_3OTFA" in HDA/OA or HDA/TOP/squalene produces Fe_3O_4 NPs, indicating that the combination of OA with TOP/squalane reduces Fe^{3+} to Fe^{2+}. Interestingly, in addition to the popcorn-shaped Fe_xO, a second phase of highly monodisperse wüstite NPs appears when using slightly increased amounts of OA/HDA and synthesis time (Figure S10). Herein, we focused on the synthesis of popcorn-shaped NPs as this novel structure offers a unique morphology by combining approximately 14 nm large subparticles into clusters measuring up to 60 nm. The individual crystallite size was determined by Rietveld refinement (Figure S11) using a Si standard reference (NBS, no. 640, PDF 027–1402) to deconvolute the instrumental broadening. Such clusters, unlike completely fused nanocrystals, still provide a large surface area, but further agglomeration seems inhibited. Additionally, they have intrinsic channels that can be visualized by TEM tomography (Figure 1c and Video S1).

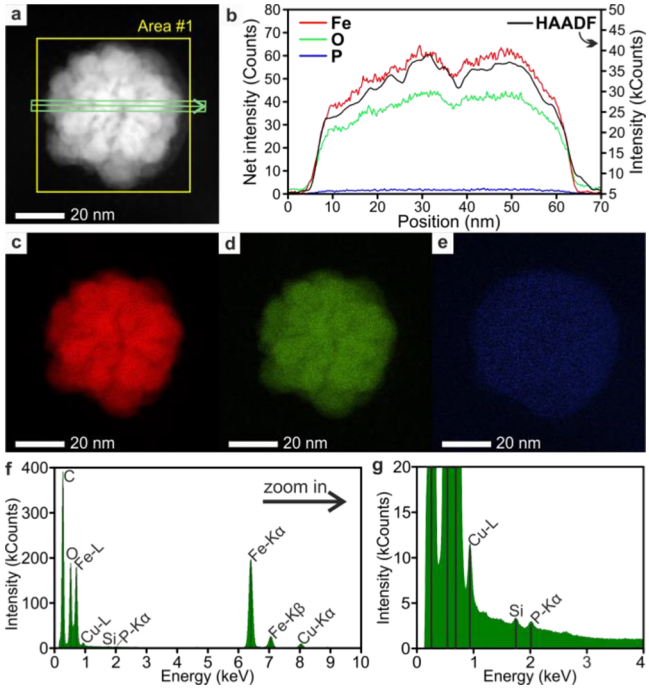

Figure 3. Elemental mapping using EDX measurements of Fe_xO nanoparticle in the HAADF-STEM mode. (a) STEM image of a Fe_xO nanoparticle. The yellow frame shows the area #1, from where the integrated STEM EDX spectra (see f and g) were extracted. The green line (integrated) shows the taken line profiles of the background corrected peak intensities. (b) Line profiles representing intensity distribution of Fe (red), O (green), P (blue), and HAADF (black). The elemental maps of the Fe_xO particle for (c) Fe, (d) O, and (e) P. (f) Integrated STEM EDX spectrum taken from the yellow area #1 indicated in a. (g) Zoom into the STEM EDX spectrum showing a minor peak of P, which is 200 times smaller than the Fe–Kα peak. Cu arises from the sample holder (Cu grids) and the small Si peak from the detector.

For magnetic iron oxide-based NPs the combined effect of the granularity and the coexistence of the antiferromagnetic wüstite and uncompensated surface spins or surface oxides (γ-Fe_2O_3 and/or Fe_3O_4) can overcome the superparamagnetic magnetic limit due to the exchange bias arising at the interface of the oxides,[43] and by reducing the thermal tumbling of small subparticles because the cluster holds them in place. The phase composition of these Fe_xO NPs remained constant for weeks. To obtain more insights into the properties of the wüstite NPs and the precursor ("Fe_3OTFA"), we conducted magnetic measurements.

Figure 4a shows the magnetic susceptibility of the precursor "Fe_3OTFA", plotted as the χT product as a function of the temperature. χT at 300 K is 5.3 emu K mol^{-1}, and it decreases to 0.45 emu K mol^{-1} at 2 K. The room temperature value is lower than expected for three uncoupled spins $s_i = 5/2$ of high-spin Fe^{3+} ions, $\chi T = 13.125$ emu K mol^{-1} (for $g_i = 2$). This lower-than-expected value at RT and the steady decrease in χT with decreasing temperature indicate strong antiferromagnetic interactions between the high-spin Fe^{3+} ions. The magnetic properties of a polynuclear spin-only complex can be modeled based on the spin Hamiltonian, as shown in eq. 1:[44]

DOI: 10.1021/acs.chemmater.7b04382
Chem. Mater. 2018, 30, 1249–1256

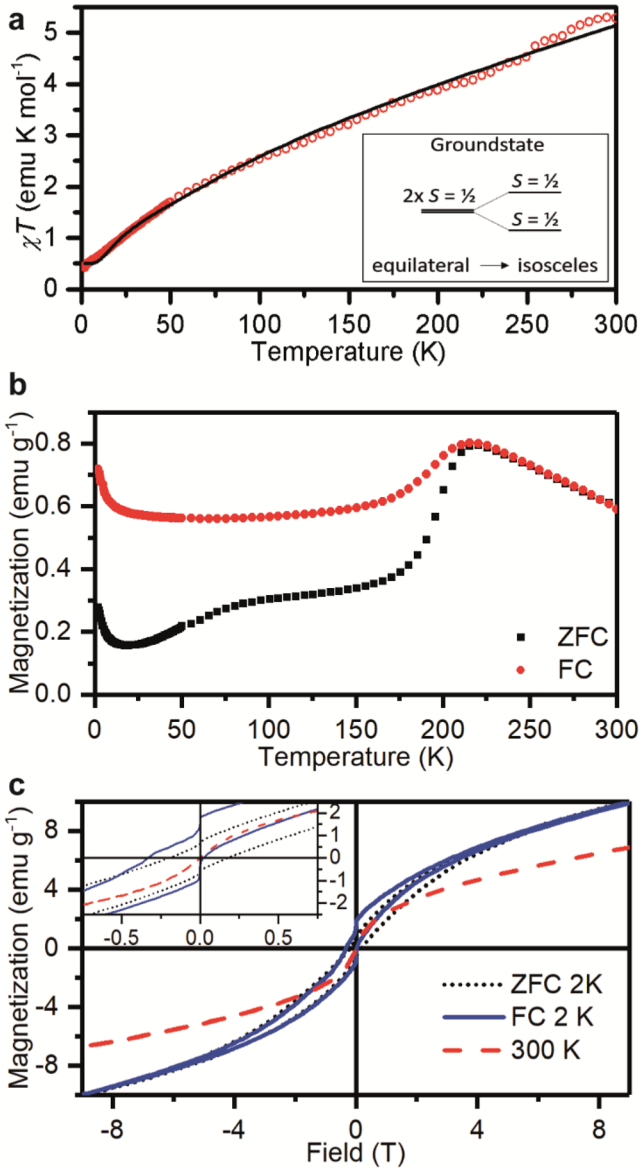

Figure 4. (a) Magnetic susceptibility (as the χT product) of "Fe_3OTFA" vs temperature. Solid line: best fit to the Hamiltonian (eq 1) with parameters $g_i = 2.32$, $J_{12} = J_{13} = -28.7$ cm^{-1}, $J_{23} = -43.2$ cm^{-1}. Inset: ground state of an equilateral (frustrated) and an isosceles triangle. (b) Magnetization vs temperature of popcorn-shaped Fe_xO ($x \approx 0.94$) NPs at 0.1 T, zero-field-cooled (ZFC, black squares) and field-cooled (FC, red circles). (c) Magnetization vs magnetic field of Fe_xO NPs at 2 K after zero-field cooling (ZFC, dotted black line) and after cooling in a field of 1 T (FC, solid blue line); magnetization at 300 K (red dashed line). Inset: expanded region around the origin.

$$\mathcal{H} = -2\sum_{i\neq j} J_{ij}\vec{s_i}\vec{s_j} + \sum_i g_i\vec{s_i}\mu_B\vec{H} \quad (1)$$

where J_{ij} are the exchange coupling constants, $\vec{s_i}$ are the spin operators, g_i are the Landé factors, μ_B is the Bohr magneton and $\vec{H}$ is the magnetic field vector. Using PHI,[45] the data can be fit based on eq 1 with i,j = 1,2,3 enumerating the Fe^{3+} ions. The best fit, shown as a solid black line (Figure 4a), was obtained with $J_{12} = J_{13} = -28.7$ cm^{-1}, $J_{23} = -43.2$ cm^{-1}, and $g_1 = g_2 = g_3 = 2.32$, comparable to a recently studied oxygen-centered Fe^{3+} triangle.[46] This fit represents an isosceles triangle. While the symmetry of the "Fe_3OTFA" core is low enough that three different exchange coupling constants and three different g-values could be used, such a model does not improve the fit significantly but instead overparameterizes the model. An argument can be made for an isosceles triangle based on the coordination of the Fe^{3+} ions: one has a different coordination than the other two (trifluoroacetates *vs* water trans to the central oxygen atom). Therefore, the complex contains two interactions between dissimilar Fe^{3+} ions and one between similar ones. Antiferromagnetic interactions in a triangle cannot all be satisfied at the same time; they are in competition. In an equilateral triangle, i.e., where all three exchange coupling parameters are the same, the molecule is spin frustrated with a doubly degenerate $S = 1/2$ ground state, which is unstable toward distortion or higher order exchange interactions (e.g., Dzyaloshinskii-Moriya interactions). In "Fe_3OTFA", the degeneracy is lifted by the unequal interactions in the triangle, leading to a gap between the two lowest $S = 1/2$ states (inset of Figure 4a).[46]

The magnetic properties of Fe_xO NPs are presented in Figure 4b. Both the zero-field-cooled (ZFC) and field-cooled (FC) magnetization, at a field of 0.1 T between 300 and 2 K, show a broad maximum at approximately 220 K and a decrease below 200 K, which is steeper in the ZFC curve. The FC magnetization is almost flat between 150 and 25 K, after which a relatively steep increase occurs with decreasing temperatures. The ZFC magnetization is only flat down to 100 K, followed by a decrease trending to zero. Below 25 K, however, an increase similar to that in the FC magnetization is observed. The broad maxima at 220 K and the sharp drop below 200 K are a clear indication of the antiferromagnetic order known for wüstite, which has a Néel temperature of ~200 K. In bulk Fe_xO, T_N increases from 192.4 to 199.2 K between $x = 0.95$ and 0.929.[47,48] Therefore, $T_N \approx 200$ K for our Fe_xO NPs is slightly higher than expected, possibly indicating some nanosize effects. The divergence of the ZFC and FC magnetization below the Néel temperature, however, is unexpected for an antiferromagnet but indicative of superparamagnetism, ferromagnetism or spin-glass freezing. The increase at low temperatures can probably be ascribed to a paramagnetic impurity with a Curie or Curie−Weiss temperature-dependence of the magnetization.

The field-dependence of the magnetization at 2 K shows a clear opening around the origin, i.e., magnetic hysteresis. While the hysteresis after ZFC is symmetrical around zero, it is shifted to negative fields after cooling in a +1 T field. The coercive field of the 2 K ZFC magnetization is ±0.2 T. The negative FC coercive field is −0.32 T, and the positive side almost goes through the origin (0.02 T). Between 2 and 200 K, the FC coercivity narrows with increasing temperature (Figures S12 and S13) and disappears by 300 K. The opening of a hysteresis at a low temperature supports superparamagnetism as an explanation for the ZFC-FC divergence. The shift of the hysteresis curve after field-cooling is reminiscent of exchange bias.[43,49] Put together, these observations indicate that the Fe_xO NPs can be viewed as antiferromagnetic cores with uncompensated surface spins. The surface spins lead to a net magnetic moment in the NPs. Due to the coupling of the surface spins to the antiferromagnetic core of the NPs, these surface spins have a preferred orientation and can be frozen in that orientation below the Néel temperature. That the hysteresis curves never saturate, not even at 9 T and 2 K, may also be attributed to the antiferromagnetic core of the Fe_xO NPs. Similar effects have been observed in NiO and CuO

DOI: 10.1021/acs.chemmater.7b04382
Chem. Mater. 2018, 30, 1249−1256

NPs[50,51] but also in Fe_xO/Fe_3O_4 core−shell NPs.[52−55] We cannot entirely rule out the partial oxidation of the Fe_xO surface leading to a similar core−shell structure, as in earlier publications.[52−55] In our case, however, any hypothetical oxidized phase is below the detection limit of powder XRD and is invisible in TEM. The presence of an exchange bias alone might not be a sufficient evidence for the oxidation of the surface to form Fe_xO/Fe_3O_4 core−shell NPs, as the examples of NiO and CuO NPs indicate.[50,51]

CONCLUSIONS

A gram-scale synthesis of a phase-pure iron oxo-trifluoroacetic precursor $[Fe_3(\mu_3\text{-}O)(CF_3COO)(\mu\text{-}CF_3COO)_6(H_2O)_2]\cdot CF_3COOH$ and its crystal structure are presented. Besides this "Fe_3OTFA" compound, three additional compounds were obtained by slight variations of the reaction conditions or crystallization procedure. "Fe_3OTFA" had been then used as a single-source precursor to obtain colloidal wüstite Fe_xO NPs by decomposition in a high-boiling solvent. These wüstite NPs show an unprecedented popcorn morphology that offers large surface area and internal channels. A 3-D tomography model created from HAADF-STEM images reveals the striking details of these popcorn-shaped Fe_xO NPs (see Video S1). Magnetic measurements of the Fe_xO NPs show signs of the antiferromagnetic order expected for wüstite but also shows a divergence of the FC and ZFC magnetizations below T_N, hysteretic magnetization curves and exchange bias. The magnetism of the precursor, "Fe_3OTFA", can be modeled by an isosceles antiferromagnetic triangle.

ASSOCIATED CONTENT

Supporting Information

The Supporting Information is available free of charge as PDF on the ACS Publications Web site. The Supporting Information is available free of charge on the ACS Publications website at DOI: 10.1021/acs.chemmater.7b04382.

Additional experimental details and crystallographic information(PDF)

Movie S1, video of the HAADF-STEM images (MPG)

Crystallographic parameters of $[Fe_3(\mu_3\text{-}O)(CF_3COO)(\mu\text{-}CF_3COO)_6(H_2O)_2]\cdot CF_3COOH$ ("Fe_3OTFA", CCDC 1559925) (CIF)

Crystallographic parameters of $[Fe_3(\mu_3\text{-}O)(\mu\text{-}CF_3COO)_6(H_2O)_3][FeCl_4]$ (CCDC 1559926) (CIF)

Crystallographic parameters of $[Fe_4(\mu_3\text{-}O)_2(CF_3COO)_4(\mu\text{-}CF_3COO)_4(H_2O)_6]\cdot 2H_2O$ (CCDC 1559927) (CIF)

Crystallographic parameters of $[Fe_3(CF_3COO)_2(\mu\text{-}CF_3COO)_4(CF_3COOH)_2(H_2O)_2(\mu\text{-}H_2O)_2]\cdot 2CF_3COOH$ (CCDC 1559928) (CIF)

AUTHOR INFORMATION

Corresponding Author

*E-mail: mvkovalenko@ethz.ch.

ORCID

Maksym V. Kovalenko: 0000-0002-6396-8938

Author Contributions

All authors have given approval to the final version of the manuscript.

Notes

The authors declare no competing financial interest.

ACKNOWLEDGMENTS

This work was financially supported by the Swiss Federal Commission for Technology and Innovation (CTI) through the Swiss Competence Centers for Energy Research (SCCER, "Heat and Electricity Storage") and the Competence Center for Energy and Mobility (CCEM, Project SLIB). R.E. acknowledges also funding from the European Research Council (ERC) under EU's Horizon 2020 programme (grant agreement 681312).

REFERENCES

(1) Arami, H.; Khandhar, A.; Liggitt, D.; Krishnan, K. M. In Vivo Delivery, Pharmacokinetics, Biodistribution and Toxicity of Iron Oxide Nanoparticles. *Chem. Soc. Rev.* **2015**, *44*, 8576−607.

(2) Liu, C.; Hajagos, T. J.; Kishpaugh, D.; Jin, Y.; Hu, W.; Chen, Q.; Pei, Q. Facile Single-Precursor Synthesis and Surface Modification of Hafnium Oxide Nanoparticles for Nanocomposite γ-Ray Scintillators. *Adv. Funct. Mater.* **2015**, *25*, 4607−16.

(3) Xing, J.; Yan, F.; Zhao, Y.; Chen, S.; Yu, H.; Zhang, Q.; Zeng, R.; Demir, H. V.; Sun, X.; Huan, A.; Xiong, Q. High-Efficiency Light-Emitting Diodes of Organometal Halide Perovskite Amorphous Nanoparticles. *ACS Nano* **2016**, *10* (7), 6623−30.

(4) Kravchyk, K.; Protesescu, L.; Bodnarchuk, M. I.; Krumeich, F.; Yarema, M.; Walter, M.; Guntlin, C.; Kovalenko, M. V. Monodisperse and Inorganically Capped Sn and Sn/SnO2 Nanocrystals for High-Performance Li-ion Battery Anodes. *J. Am. Chem. Soc.* **2013**, *135*, 4199−202.

(5) You, J.; Meng, L.; Song, T. B.; Guo, T. F.; Yang, Y. M.; Chang, W. H.; Hong, Z.; Chen, H.; Zhou, H.; Chen, Q.; Liu, Y.; De Marco, N.; Yang, Y. Improved Air Stability of Perovskite Solar Cells via Solution-Processed Metal Oxide Transport Layers. *Nat. Nanotechnol.* **2016**, *11*, 75−81.

(6) Hazen, R. M.; Jeanloz, R. Wüstite ($Fe_{1-x}O$): A Review of Its Defect Structure and Physical Properties. *Rev. Geophys.* **1984**, *22*, 37−46.

(7) Günther, P. L.; Rehaag, H. Über die Thermische Zersetzung von Oxalaten. *Z. Anorg. Allg. Chem.* **1939**, *243*, 60−68.

(8) Darken, L. S.; Gurry, R. W. The System Iron-Oxygen. I. The Wüstite Field and Related Equilibria. *J. Am. Chem. Soc.* **1945**, *67*, 1398−1412.

(9) Yin, M.; O'Brien, S. Synthesis of Monodisperse Nanocrystals of Manganese Oxides. *J. Am. Chem. Soc.* **2003**, *125*, 10180−81.

(10) Willis, B. T. M.; Rooksby, H. P. Change of Structure of Ferrous Oxide at Low Temperature. *Acta Crystallogr.* **1953**, *6*, 827−831.

(11) Sun, X.; Frey Huls, N.; Sigdel, A.; Sun, S. Tuning Exchange Bias in Core/Shell FeO/Fe_3O_4 Nanoparticles. *Nano Lett.* **2012**, *12*, 246−251.

(12) Khurshid, H.; Li, W.; Chandra, S.; Phan, M. H.; Hadjipanayis, G. C.; Mukherjee, P.; Srikanth, H. Mechanism and Controlled Growth of Shape and Size Variant Core/Shell FeO/Fe_3O_4 Nanoparticles. *Nanoscale* **2013**, *5*, 7942−52.

(13) Leszczyński, B.; Hadjipanayis, G. C.; El-Gendy, A. A.; Załęski, K.; Śniadecki, Z.; Musiał, A.; Jarek, M.; Jurga, S.; Skumiel, A. The Influence of Oxidation Process on Exchange Bias in Egg-Shaped FeO/Fe_3O_4 Core/Shell Nanoparticles. *J. Magn. Magn. Mater.* **2016**, *416*, 269−274.

(14) Redl, F. X.; Black, C. T.; Papaefthymiou, G. C.; Sandstrom, R. L.; Yin, M.; Zeng, H.; Murray, C. B.; O'Brien, S. P. Magnetic, Electronic, and Structural Characterization of Nonstoichiometric Iron Oxides at the Nanoscale. *J. Am. Chem. Soc.* **2004**, *126*, 14583−599.

(15) Hou, Y.; Xu, Z.; Sun, S. Controlled Synthesis and Chemical Conversions of FeO Nanoparticles. *Angew. Chem.* **2007**, *119*, 6445−48.

(16) Bronstein, L. M.; Atkinson, J. E.; Malyutin, A. G.; Kidwai, F.; Stein, B. D.; Morgan, D. G.; Perry, J. M.; Karty, J. A. Nanoparticles by Decomposition of Long Chain Iron Carboxylates: From Spheres to Stars and Cubes. *Langmuir* **2011**, *27*, 3044−50.

DOI: 10.1021/acs.chemmater.7b04382
Chem. Mater. 2018, 30, 1249−1256

(17) Bronstein, L. M.; Huang, X.; Retrum, J.; Schmucker, A.; Pink, M.; Stein, B. D.; Dragnea, B. Influence of Iron Oleate Complex Structure on Iron Oxide Nanoparticle Formation. *Chem. Mater.* **2007**, *19*, 3624−32.
(18) Yin, M.; Chen, Z.; Deegan, B.; O'Brien, S. Wüstite Nanocrystals: Synthesis, Structure and Superlattice Formation. *J. Mater. Res.* **2007**, *22*, 1987−95.
(19) Wetterskog, E.; Tai, C. W.; Grins, J.; Bergstrom, L.; Salazar-Alvarez, G. Anomalous magnetic properties of nanoparticles arising from defect structures: topotaxial oxidation of Fe(1-x)O|Fe(3-delta)O4 corelshell nanocubes to single-phase particles. *ACS Nano* **2013**, 7 (8), 7132−44.
(20) Bodnarchuk, M. I.; Kovalenko, M. V.; Groiss, H.; Resel, R.; Reissner, M.; Hesser, G.; Lechner, R. T.; Steiner, W.; Schaffler, F.; Heiss, W. Exchange-Coupled Bimagnetic Wüstite/Metal Ferrite Core/Shell Nanocrystals: Size, Shape, and Compositional Control. *Small* **2009**, *5*, 2247−52.
(21) Bodnarchuk, M. I.; Kovalenko, M. V.; Pichler, S.; Fritz-Popovski, G.; Hesser, G.; Heiss, W. Large-Area Ordered Superlattices from Magnetic Wüstite/Cobalt Ferrite Core/Shell Nanocrystals by Doctor Blade Casting. *ACS Nano* **2010**, *4*, 423−431.
(22) Dolomanov, O. V.; Bourhis, L. J.; Gildea, R. J.; Howard, J. A. K.; Puschmann, H. Olex2: A Complete Structure Solution, Refinement and Analysis Program. *J. Appl. Crystallogr.* **2009**, *42* (2), 339−341.
(23) Sheldrick, G. M. A Short History of SHELX. *Acta Crystallogr., Sect. A: Found. Crystallogr.* **2008**, *64* (Pt 1), 112−122.
(24) Palatinus, L.; Chapuis, G. Superflip− A Computer Program for the Solution of Crystal Structures by Charge Flipping in Arbitrary Dimensions. *J. Appl. Crystallogr.* **2007**, *40* (4), 786−790.
(25) Palatinus, L.; van der Lee, A. Symmetry Determination Following Structure Solution in P1. *J. Appl. Crystallogr.* **2008**, *41* (6), 975−984.
(26) Palatinus, L.; Prathapa, S. J.; van Smaalen, S. r. EDMA: A Computer Program for Topological Analysis of Discrete Electron Densities. *J. Appl. Crystallogr.* **2012**, *45* (3), 575−580.
(27) Sheldrick, G. M. Crystal Structure Refinement with SHELXL. *Acta Crystallogr., Sect. C: Struct. Chem.* **2015**, *71* (1), 3−8.
(28) Iranpoor, N.; Adibi, H. Iron(III) Trifluoroacetate as an Efficient Calatyst for Solvolytic and Nonsolvolytic Nucleaphilic Ring Opening of Epoxides. *Bull. Chem. Soc. Jpn.* **2000**, *73*, 675−680.
(29) Adibi, H.; Samimi, H. A.; Beygzadeh, M. Iron(III) Trifluoroacetate and Trifluoromethanesulfonate: Recyclable Lewis Acid Catalysts for One-Pot Synthesis of 3,4-Dihydropyrimidinones or their Sulfur Analogues and 1,4-Dihydropyridines via Solvent-Free Biginelli and Hantzsch Condensation Protocols. *Catal. Commun.* **2007**, *8*, 2119−2124.
(30) Ertürk, E.; Demir, A. S. Iron(III) Trifluoroacetate [Fe-$(O_2CCF_3)_3$] Catalyzed Epoxide Opening with Amines. *ARKIVOC* **2008**, *2*, 160−171.
(31) Zhang, M.; Wang, T.; Xiong, B.; Yan, F.; Wang, X.; Ding, Y.; Song, Q. Efficient Synthesis of 2,4-Diarylquinolines via Fe(III) Trifluoroacetate Catalyzed Three-Component Reactions under Solvent-Free Conditions. *Heterocycles* **2012**, *85*, 639−649.
(32) Zhang, M.; Xiong, B.; Yang, W.; Chen, L.; Wu, F.; Wang, Q.; Ding, Y. Highly Efficient One-Pot, Three-Component Synthesis of β-Aminoketones Catalyzed by $Fe(O_2CCF_3)_3$. *Synth. Commun.* **2012**, *42*, 2831−43.
(33) Adibi, H.; Samimi, H. A.; Iranpoor, N. Iron(III) Trifluoroacetate: Chemoselective and Recyclable Lewis Acid Catalyst for Diacetylation of Aldehydes, Thioacetalization and Transthioacetalization of Carbonyl Compounds and Aerobic Coupling of Thiols. *Chin. J. Chem.* **2008**, *26*, 2086−2092.
(34) Firouzabadi, H.; Iranpoor, N.; Jafari, A. A.; Jafari, M. R. Iron(III) Trifluoroacetate $[Fe(F_3CCO_2)_3]$ as an Easily Available, Non-Hygroscopic, Non-Corrosive, Highly Stable and a Reusable Lewis Acid Catalyst: Efficient *O*-Silylation of Alpha-Hydroxyphosphonates, Alcohols and Phenols by Hexamethyldisilazane (HMDS) under Solvent-Free Conditions. *J. Organomet. Chem.* **2008**, *693*, 2711−2714.
(35) Ertürk, E.; Göllü, M.; Demir, A. S. Efficient Rearrangement of Epoxides Catalyzed by a Mixed-Valent Iron Trifluoroacetate $[Fe_3O(O_2CCF_3)_6(H_2O)_3]$. *Tetrahedron* **2010**, *66*, 2373−77.
(36) Guntlin, C. P.; Zünd, T.; Kravchyk, K. V.; Wörle, M.; Bodnarchuk, M. I.; Kovalenko, M. V. Nanocrystalline FeF_3 and MF_2 (M = Fe, Co, and Mn) from Metal Trifluoroacetates and Their Li(Na)-Ion Storage Properties. *J. Mater. Chem. A* **2017**, *5*, 7383−93.
(37) Tapper, A. E.; Long, J. R.; Staples, R. J.; Stavropoulos, P. Oxygenation of Hydrocarbons Mediated by Mixed-Valent Basic Iron Trifluoroacetate and Valence-Separated Component Species under Gif-Type Conditions Involves Carbon- and Oxygen-Centered Radicals. *Angew. Chem.* **2000**, *112*, 2433−36.
(38) Glazunova, T. Y.; Boltalin, A. I.; Troyanov, S. I. Synthesis and Crystal Structure of Trinuclear Carboxylate Complexes $M_3(\mu_3\text{-}O)(CF_3COO)_6L_3$. *Mendeleev Commun.* **2004**, *14*, 141−143.
(39) Ponomarev, V. I.; Filipenko, O. S.; Atovmyan, L. O.; Bobkova, S. A.; Turte, K. I. Crystal Structure of Trinuclear Trifluoroacetate Complex of Mixed-Valency Iron $[Fe_3O(O_2CCF_3)_6(H_2O)_3]\cdot 3.5H_2O$. *Dokl. Akad. Nauk SSSR* **1981**, *262*, 346−350.
(40) Qian, C.; Kim, F.; Ma, L.; Tsui, F.; Yang, P.; Liu, J. Solution-Phase Synthesis of Single-Crystalline Iron Phosphide Nanorods/Nanowires. *J. Am. Chem. Soc.* **2004**, *126*, 1195−1198.
(41) Komura, K.; Nakano, Y.; Koketsu, M. Mesoporous Silica MCM-41 as a Highly Active, Recoverable and Reusable Catalyst for Direct Amidation of Fatty Acids and Long-Chain Amines. *Green Chem.* **2011**, *13*, 828−831.
(42) Sugi, Y.; Terada, Y.; Ieda, N.; Komura, K. Multivalent Metal Salts as Versatile Catalysts for the Amidation of Long-Chain Aliphatic Acids with Aliphatic Amines. *Synthesis* **2008**, *2008* (15), 2318−2320.
(43) Skumryev, V.; Stoyanov, S.; Zhang, Y.; Hadjipanayis, G.; Givord, D.; Nogues, J. Beating the Superparamagnetic Limit with Exchange Bias. *Nature* **2003**, *423*, 850−853.
(44) Kahn, O. *Molecular Magnetism*; Wiley: Weinheim: Germany, 1993.
(45) Chilton, N. F.; Anderson, R. P.; Turner, L. D.; Soncini, A.; Murray, K. S. PHI: a Powerful New Program for the Analysis of Anisotropic Monomeric and Exchange-Coupled Polynuclear *d*- and *f*-Block Complexes. *J. Comput. Chem.* **2013**, *34*, 1164−75.
(46) Georgopoulou, A. N.; Margiolaki, I.; Psycharis, V.; Boudalis, A. K. Dynamic versus Static Character of the Magnetic Jahn-Teller Effect: Magnetostructural Studies of $[Fe_3O(O_2CPh)_6(py)_3]ClO_4$·py. *Inorg. Chem.* **2017**, *56*, 762−772.
(47) Seehra, M. S.; Srinivasan, G. Magnetic Studies of non-Stoichiometric Fe_zO and Evidence for Magnetic Defect Clusters. *J. Phys. C: Solid State Phys.* **1984**, *17*, 883−892.
(48) McCammon, C. A. Magnetic Properties of Fe_xO ($x > 0.95$): Variation of Néel Temperature. *J. Magn. Magn. Mater.* **1992**, *104*, 1937−1938.
(49) Nogués, J.; Schuller, I. K. Exchange Bias. *J. Magn. Magn. Mater.* **1999**, *192*, 203−232.
(50) Kodama, R. H.; Makhlouf, S. A.; Berkowitz, A. E. Finite Size Effects in Antiferromagnetic NiO Nanoparticles. *Phys. Rev. Lett.* **1997**, *79*, 1393−96.
(51) Punnoose, A.; Magnone, H.; Seehra, M. S.; Bonevich, J. Bulk to Nanoscale Magnetism and Exchange Bias in CuO Nanoparticles. *Phys. Rev. B: Condens. Matter Mater. Phys.* **2001**, *64*, 174420−8.
(52) Pichon, B. P.; Gerber, O.; Lefevre, C.; Florea, I.; Fleutot, S.; Baaziz, W.; Pauly, M.; Ohlmann, M.; Ulhaq, C.; Ersen, O.; Pierron-Bohnes, V. r.; Panissod, P.; Drillon, M.; Begin-Colin, S. Microstructural and Magnetic Investigations of Wüstite-Spinel Core-Shell Cubic-Shaped Nanoparticles. *Chem. Mater.* **2011**, *23*, 2886−900.
(53) Sharma, S. K.; Vargas, J. M.; Pirota, K. R.; Kumar, S.; Lee, C. G.; Knobel, M. Synthesis and Ageing Effect in FeO Nanoparticles: Transformation to core−shell FeO/Fe_3O_4 and Their Magnetic Characterization. *J. Alloys Compd.* **2011**, *509*, 6414−17.
(54) Lak, A.; Kraken, M.; Ludwig, F.; Kornowski, A.; Eberbeck, D.; Sievers, S.; Litterst, F. J.; Weller, H.; Schilling, M. Size Dependent Structural and Magnetic Properties of FeO-Fe_3O_4 Nanoparticles. *Nanoscale* **2013**, *5*, 12286−95.

DOI: 10.1021/acs.chemmater.7b04382
Chem. Mater. 2018, 30, 1249−1256

(55) Khurshid, H.; Chandra, S.; Li, W.; Phan, M. H.; Hadjipanayis, G. C.; Mukherjee, P.; Srikanth, H. Synthesis and Magnetic Properties of Core/Shell FeO/Fe_3O_4 Nano-Octopods. *J. Appl. Phys.* **2013**, *113*, 17B508.

DOI: 10.1021/acs.chemmater.7b04382
Chem. Mater. 2018, 30, 1249−1256